Article citation info:
Lei S. Centrifugal pump efficiency enhancement and fault diagnosis methods based on digital twins. Diagnostyka. 2026;27(3):2026305.
https://doi.org/10.29354/diag/226130.

DIAGNOSTYKA, 2026, Vol. 27, No. 3

e-ISSN 2449-5220
DOI: 10.29354/diag/226130

CENTRIFUGAL PUMP EFFICIENCY ENHANCEMENT AND FAULT DIAGNOSIS METHODS BASED ON DIGITAL TWINS

Shun'an LEI

School of Petrochemical Engineering, Guangzhou Institute of Technology, Guangzhou, 510725, China
* Corresponding author, e-mail: shunan2025@163.com

Abstract

Centrifugal pumps often suffer from low operating efficiency and present challenges in accurately diagnosing impeller blade fracture faults. Therefore, this study develops a method for improving centrifugal pump efficiency and diagnosing faults based on digital twins. For efficiency improvement, a digital twin optimization framework for the centrifugal pump impeller is established. Initial samples are generated through Latin hypercube sampling, and a surrogate model is constructed by combining computational fluid dynamics numerical simulations with an approximate model. A PSO algorithm is applied to solve a multi-objective programming problem with the objectives of minimizing entropy production and maximizing efficiency. For fault diagnosis, the generated pressure and velocity contour map datasets are input into a target detection network for training, and subsequently, a stacked ensemble strategy is introduced to fuse the two types of detection results for decision-making. The findings reveal that the optimized impeller's hydraulic efficiency is improved by 4.6%, while entropy production is reduced by 18.6%. The proposed method can enhance centrifugal pumps' performance and achieve accurate diagnosis of blade fracture faults, thereby providing a new technical path for intelligent efficiency improvement and accurate fault diagnosis of centrifugal pumps.

Keywords: Digital twin; Centrifugal pump; Particle swarm optimization algorithm; Target detection network; Fault diagnosis

1. INTRODUCTION

Centrifugal pumps (CPs), as the core power equipment of the process industry, play an irreplaceable role in key areas of the national economy such as petrochemicals, power energy, and water treatment [1]. CPs operate under complex conditions for a long time, and the impeller blades are prone to fracture due to fatigue, cavitation and other factors, which leads to performance degradation and serious safety accidents [2]. Therefore, improving the operating efficiency of CPs and achieving accurate diagnosis of impeller mechanical faults has become a key area of research in the intelligent operation and maintenance of process industry equipment [3]. In terms of improving efficiency and transforming processes, although computational fluid dynamics (CFD) technology has provided a way for designing CPs hydraulically, it is still difficult to fully explore optimal solutions in the design space with a single CFD simulation, and the calculation cost is high [4]. In terms of Fault Diagnosis (FD), traditional methods are mostly based on vibration signal analysis, and fault identification is achieved through time-frequency domain feature extraction and pattern recognition [5]. However, the installation of acceleration sensors is limited in some working scenarios, and vibration signals under complex conditions will exhibit nonlinear and non-stationary characteristics, and fault characteristics are easily submerged by environmental noise [6]. The rise of Digital Twin (DT) technology has supported a new way to solving the above problems. As a core technology for achieving the deep integration of cyber-physical systems, it allows real-time monitoring, simulation, prediction and optimization of equipment decisions [7].

Against this background, this study develops an integrated method for improving the efficiency of CPs and diagnosing faults based on DTs. The goal is to furnish CPs and accurate FD with theoretical support and technical reference, and to encourage the in-depth use of DTs in the field of fluid machinery.

2. RELATED WORKS

DT technology, as a core means of realizing cyber-physical integration, has received widespread attention and application exploration in the field of CPs in recent years. This technology realizes real-time mapping, simulation prediction and optimization decision-making of the entire life cycle of physical entities by constructing a high-fidelity

Received 2026-05-21; Accepted 2026-07-15; Available online 2026-07-15

virtual model of the physical entity[8]. Zhou et al. proposed a dynamic pump station scheduling method based on DTs, which uses DT technology to predict the available status of pump units in advance and trigger the rescheduling process in a timely manner. The findings reveal that the average energy saving rate reaches 9.78% under the premise of ensuring dynamic water balance, thereby ensuring the high efficiency and stability of pump station operation [9]. Li et al. designed a method for constructing a monitoring system grounded on DTs to meet the needs of smart monitoring and prediction for CP turbines. This method constructs a twin virtual model through dimensionality reduction theory and uses point cloud technology and Unity3D platform to realize system visualization. The outcomes demonstrate that the model can effectively realize cavitation prediction and state cloud map drawing [10].

The hydraulic design method of CPs has evolved from empirical design to numerical simulation and then to intelligent optimization. The traditional velocity coefficient method mainly relies on the designer's experience and existing model pumps, which makes it difficult to break through the performance bottleneck of the original design [11]. With the development of CFD, researchers have begun to use CFD technology to accurately simulate the internal flow of CPs. However, single CFD simulation is still difficult to fully explore the global optimal solution in the design space, which limits its application efficiency in iterative optimization [12]. Therefore, researchers have introduced intelligent optimization algorithms into the field of CP optimization design. Zhao et al. utilized Spearman's rank correlation analysis to screen key parameters, constructed a high-precision alternative model through a genetic algorithm and a BPNN, and optimized it using a multi-island GA. Their findings suggest that the rated point efficiency of the optimized model increased by 4.29% [13]. Li et al. designed an automatic optimization method grounded on an adaptive single-objective algorithm and CFD. This method applies optimal space-filling experimental design to screen the set of parameters and combines Kriging response surfaces and mixed-integer sequential quadratic programming for optimization. The findings suggest that the efficiency of the optimised pump increased by 2.75% [14].

CPFD is traditionally grounded on vibration signal analysis. Vibration signals are collected by accelerometers, and time-frequency domain features are extracted for fault identification [15]. However, it is sometimes difficult to obtain vibration signals, and there is a lot of noise in the industrial field, which can easily drown out the actual fault signals, increasing the difficulty of diagnosis [16]. Driven by the deep learning technology, CPFD has shifted towards an end-to-end smart diagnosis mode grounded on DNNs. Siddique et al. developed a CPFD method grounded on deep learning that enhances vibration signal features using a non-local mean filter. It then inputs the scale map into a CNN to extract features for fault identification. The findings demonstrate that this method achieves a classification accuracy of over 99.86% [17]. Manikandan S and Duraivelu K proposed a deep CNN FD method based on vibration signals. The signal is converted into a two-dimensional image using image processing technology and input into a deep CNN classifier for training and testing. The outcomes show that the accuracy of this method for fault identification is 99.07% [18].

Despite the progress made in the aforementioned research, the following shortcomings remain: existing efficiency-enhancing retrofit studies mostly focus on single-objective optimization; traditional FD methods rely excessively on vibration signal analysis, resulting in insufficient robustness and accuracy in fault feature extraction.

In the field of technical diagnosis, traditional CPFD methods mainly rely on vibration signal analysis, which has problems such as limited sensor installation and environmental noise interference. Although deep learning based methods have improved diagnostic accuracy, most methods lack interpretability and cannot establish a clear physical mapping between flow field characteristics and fault mechanisms. Therefore, this study proposes a diagnostic method using flow field cloud maps generated by digital twins to address the aforementioned shortcomings, providing high accuracy and physical interpretability for technical diagnosis. This study develops an integrated method for CP efficiency enhancement and FD based on DTs. By employing an approximate model and the PSO, a multi-objective optimization model is constructed to achieve global optimization of impeller hydraulic performance. The performance of CPFD is enhanced by combining a You Only Look Once version 5 (YOLOv5) target detection network with a stacking integration method. The novelty of this research lies in: constructing a model with the objectives of minimizing entropy production and maximizing efficiency; introducing Latin hypercube sampling, the Kriging approximation model, and the PSO algorithm to achieve global optimization of impeller geometry while ensuring computational efficiency; and combining a target detection network with a stacking integration strategy to strengthen the accuracy of FD.

3. METHODOLOGY

This study first proposes a CP efficiency enhancement method based on DTs and the PSO algorithm, aiming to reduce the energy loss of CPs. Then, it proposes a CPFD method that integrates target detection and stacking integration to improve the accuracy of FD.

3.1. Centrifugal pump efficiency enhancement method based on DT and PSO algorithm

CPs are the core power equipment of fluid transport systems, and their operating efficiency directly affects the energy consumption level and economy of industrial production [19]. Traditional optimization methods mostly rely on empirical design and single-objective CFD simulation, which makes it difficult to balance multi-objective collaborative optimization and the search efficiency of the global optimal solution [20]. A DT is a high-fidelity virtual mapping model of physical entities that enables real-time monitoring and simulation prediction of the entire life cycle of equipment [21]. Therefore, this study proposes a CP efficiency enhancement and modification method based on DT and PSO algorithm, aiming to maximize hydraulic efficiency and minimize energy loss. The high-fidelity digital twin model of the CP is constructed through a systematic process encompassing geometric parameterization, mesh generation, boundary condition specification, and solver configuration. The impeller and volute geometries are parameterized using CFturbo software, with structured hexahedral meshes generated in ANSYS ICEM CFD. The shear stress transport turbulence model is adopted for its superior performance in capturing near-wall flow separation and adverse pressure gradient phenomena.

The digital twin framework is practically implemented through bidirectional data integration. The physical pump's geometric and operational parameters are mapped to the virtual model, while CFD simulation results are continuously validated against experimental measurements and used to update model parameters, thereby establishing a closed-loop cyber-physical coupling that enables real-time monitoring, predictive simulation, and iterative optimization. The digital twin framework implemented in this study is constructed following a five-layer architecture encompassing physical entity, data acquisition and transmission, virtual model, data integration and synchronization, and application service layers. The physical layer consists of the CP and its associated instrumentation. The acquisition layer collects real-time operational data at a sampling rate of $1-2$ kHz through a distributed control system and transmits them to the twin platform via OPC Unified Architecture protocol. The virtual layer is established through parameterized CFD modeling in CFturbo and ANSYS CFX. The integration layer constitutes the critical distinction from conventional offline simulations. The application layer hosts the efficiency optimization and FD services. While the optimization and diagnostic algorithms were executed in an offline manner due to computational constraints, the framework architecture supports eventual online deployment. The DT technology is denoted in Figure 1.

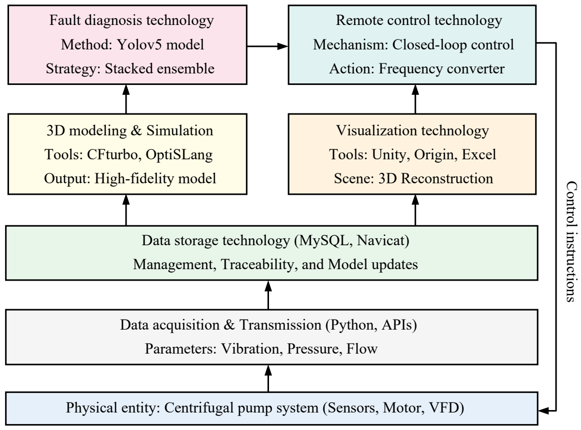

Fig. 1. Schematic diagram of DT technology

Figure 1 shows the overall architecture of DT technology in CP system. Through bidirectional mapping between physical entities and virtual models, a closed-loop process from state perception to optimization control is realized. The study established a parameterized model of CP impeller using CF turbo software, constructed an automatic optimization process using the OptiSLang platform, selected inlet diameter, outlet diameter, blade outlet width, blade inlet installation angle and outlet installation angle as optimization variables, and used the Latin hypercube sampling method to generate an initial sample set [22]. Its expression is shown in equation (1).

$$\begin{cases} \boldsymbol{x} = [D_1, D_2, b_2, \beta_1, \beta_2] \\ X = \{x^{(1)}, x^{(2)}, \dots, x^{(N)}\} \end{cases} \tag{1}$$

In equation (1), $\boldsymbol{x}$ means the design variable vector. D_1 and D_2 indicate the impeller inlet and outlet diameters. b_2 denotes the blade outlet width. β_1 and β_2 indicate the blade inlet and outlet installation angles. X is the set of sample points. $x^{(1)}$ is the first sample point. N refers to the total amount of samples. Then, the efficiency and entropy production of each sample are obtained through CFD numerical simulation. The calculation of efficiency is denoted in equation (2).

$$\eta = P_{\text{hyd}}/P_{\text{shaft}} = \rho g Q H / M\omega \tag{2}$$

In equation (2), η represents the energy conversion efficiency of the CP impeller. P_{hyd} and P_{shaft} represent the hydraulic power obtained by the fluid and the shaft power input to the impeller, respectively. ρ and g represent the fluid density and gravitational acceleration, respectively. Q and H represent the volumetric flow rate and head, respectively. M and ω represent the torque and angular velocity, respectively. The entropy production is calculated as shown in equation (3).

$$S_{\text{gen}} = \int_V \frac{\Phi}{T} dV \tag{3}$$

In equation (3), S_{gen} means the total entropy generation rate. Φ and T represent the dissipation function and temperature, respectively. V represents the fluid domain volume. Further research employs approximation techniques to reduce the computational cost of CFD simulations and achieve rapid prediction. An approximate model is built based on the Kriging model, and its expression is shown in equation (4).

$$\hat{y}(x) = \mu + \boldsymbol{r}^T(x)\boldsymbol{R}^{-1}(\boldsymbol{y} - 1\mu) \tag{4}$$

In equation (4), $\hat{y}(x)$ is the predicted value. μ stands for the global mean. $\boldsymbol{r}^T$ is the transpose of the correlation vector. $\boldsymbol{R}$ is the correlation matrix. $\boldsymbol{y}$ is the sample point response vector. A schematic diagram of the approximation technique based on the Kriging is denoted in Figure 2.

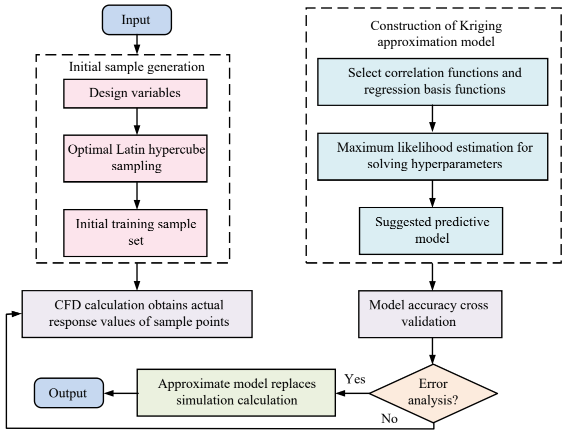

Fig. 2. Schematic diagram of approximation technique based on Kriging model

In Figure 2, the approximation technique first generates an initial sample through optimal Latin hypercube sampling, and then obtains the actual response value through CFD calculation. Then, the correlation function and regression basis function are selected, and the hyperparameters are solved using maximum likelihood estimation to construct a surrogate model. To enhance the hydraulic effectiveness of the impeller, a multi-objective programming with the objectives of minimizing entropy production and maximizing efficiency is studied and constructed. The mathematical expression of this problem is denoted in equation (5).

$$\begin{cases} min\, f_1(x) = S_{\text{gen}}(x) \\ max\, f_2(x) = \eta(x) \end{cases} \tag{5}$$

In equation (5), $min\, f_1(x)$ means the objective function to reduce entropy production. $max\, f_2(x)$ is the objective function to maximize efficiency. To solve the above multi-objective optimization problem, a PSO algorithm is introduced. Each particle updates its velocity based on its individual historical best position and the group's historical best position, as shown in equation (6).

$$v_i^{k+1} = wv_i^k + c_1r_1(p_{\text{best},i} - x_i^k) + c_2r_2(g_{\text{best}} - x_i^k) \tag{6}$$

In equation (6), v_i^{k+1} denotes the velocity of the particle i in the $k+1$ iteration. v_i^k denotes the velocity of the particle i in the current generation. w denotes the inertia weight. c_1 and c_2 indicate the individual and the social learning factors. r_1 and r_2 indicate random numbers. $p_{\text{best},i}$ means the individual historical best position of the particle i. g_{best} refers to the global best value. The position update is shown in equation (7).

$$x_i^{k+1} = x_i^k + v_i^{k+1} \tag{7}$$

In equation (7), x_i^{k+1} refers to the position of the particle $i$in the $k+1$iteration. x_i^k means the position of the particle i in the current iteration. In multi-objective optimization, Pareto optimal solutions are introduced, and the membership degree of each solution is calculated using the fuzzy comprehensive evaluation method, as shown in equation (8).

$$\begin{cases} \mu_j = \dfrac{\sum_{k=1}^{m} \mu_{jo}}{m} \\ \mu_{jo} = \dfrac{f_o^{max_{jo}}}{f_o^{max_o^{min}}} \end{cases} \tag{8}$$

In equation (8), $\mu_j$means the total satisfaction of the j -th Pareto solution. μ_{jo} is the satisfaction of the jth solution on the o -th objective. m denotes the amount of objective functions. f_{jo} is j the actual objective value of the j -th solution on the o -th objective. $f_o^{max}$and f_o^{min} indicate the max and mini values of the o -th objective among all Pareto solutions, respectively. After obtaining the Pareto-optimal solution set through the PSO algorithm, a decision-making strategy is required to select the final optimal impeller design for practical implementation. In this study, the fuzzy comprehensive evaluation method is adopted to rank the Pareto solutions and identify the best compromise between the two conflicting objectives. The overall satisfaction degree for the Pareto solution is then calculated as the arithmetic mean of the individual membership values across both objectives, and the solution with the highest value is selected as the final optimal design. Equal weights are assigned to both objectives (0.5), reflecting the practical engineering requirement that efficiency and energy loss are equally important performance indicators for CP operation. Furthermore, all geometric parameters lie well within manufacturable ranges, ensuring practical feasibility without requiring special fabrication techniques. The selected solution remains among the top two candidates under alternative weighting configurations (7:3 favoring efficiency), confirming its robustness as the preferred design choice. The Pareto optimal solution and the PSO algorithm is shown in Figure 3.

distribution of different design schemes in the target space, and the curves form the Pareto front, with all points on the front being non-dominated solutions. In Figure 3(b), starting from the initial position and velocity of the particle swarm, the initial fitness values are evaluated sequentially, followed by an iterative loop to update the particle positions and velocities, searching for individual optima and global optima. Through the above optimization framework based on DTs and the PSO algorithm, the efficiency enhancement of the CP impeller structure was achieved. This framework aims to minimize entropy production and maximize efficiency, using the Kriging approximation model to replace high-cost CFD simulation, and combining the PSO algorithm to efficiently search for Pareto optimal solutions in the global design space. The optimized impeller geometry parameters make the internal flow more uniform, reducing flow separation and eddy losses, improving hydraulic efficiency, and reducing energy dissipation. The schematic diagram of the CP impeller efficiency improvement is shown in Figure 4.

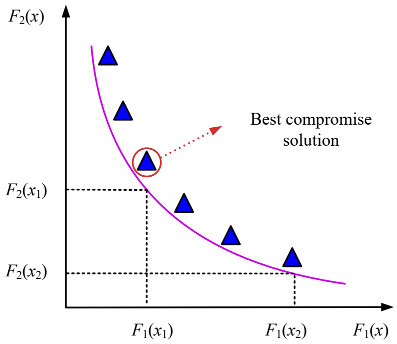

(a) Schematic diagram of Pareto optimal solution

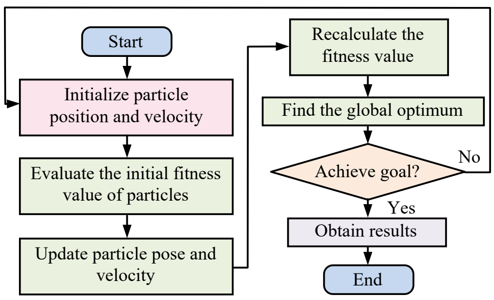

(b) The flowchart of PSO algorithm

Fig. 3. Process diagram of Pareto optimal solution and PSO algorithm

In Figure 3(a), the scatter plots represent the

Figure 4 shows a schematic diagram of the impeller structure of the CP used for efficiency improvement in this study. The research object is a single-stage single suction CP, with the following design parameters: the flow rate of the CP is $18m^3/h$, the head is 22m, the speed is 2900r/min, the inlet diameter and outlet drop are 50mm and 40mm respectively, the impeller diameter is 136mm, the number of blades is 6, and the rated power is 2.2kW. The key components such as impeller, volute, inlet and outlet are clearly marked. This structure serves as a benchmark model for subsequent multi-objective optimization based on digital twins, in order to minimize entropy production and maximize efficiency.

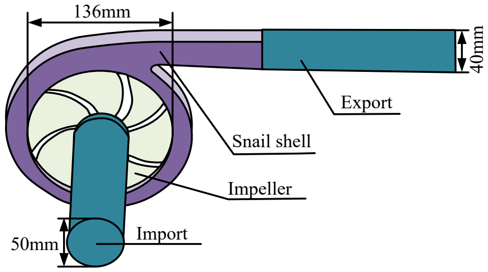

Fig. 4. Schematic diagram of centrifugal pump impeller efficiency improvement modification

3.2. A CPFD method integrating target detection and stacking integration

Based on the improvement of CP impeller efficiency, in order to further ensure its long-term stable operation under complex working conditions, it is necessary to build an efficient and robust FD mechanism [23]. In view of the problems of traditional FD methods that rely too much on vibration signals, are susceptible to noise interference and have limited sensor installation, a CPFD method that integrates target detection and stacking integration is proposed. The physical mechanism between flow field characteristics and blade fracture faults is as follows: the fractured blades disrupt the symmetrical flow pattern inside the impeller, generating local low-pressure zones and high-speed jets. These abnormal phenomena are manifested as distinguishable patterns in pressure and velocity cloud maps. The proposed method utilizes this physical mapping relationship to automatically learn and locate the flow field distortion patterns caused by faults through YOLOv5, thereby achieving accurate fault detection without relying on vibration signals. The method inputs the generated pressure cloud map and velocity cloud map into the YOLOv5 target detection network for training, identifies the fault area in the cloud map and classifies the fault type. The training of the object detection network relies on the joint optimization of the loss function (LF), which consists of bounding box regression loss, confidence

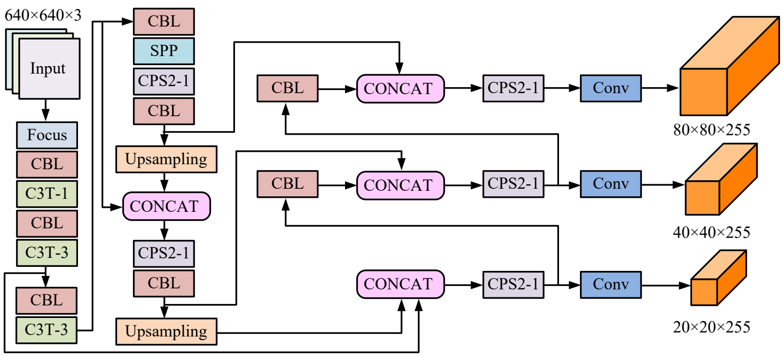

Fig. 5. Schematic diagram of Yolov5 object detection network

loss and classification loss. The bounding box regression loss is shown in equation (9) [24].

$$L_{\text{coord}} = 1 - \text{IoU} + \frac{\rho^2(b,b^{gt})}{c^2} + \alpha v \tag{9}$$

In equation (9), L_{coord} represents the bounding box regression loss. IoU means the intersection-union ratio (IU/U) of the predicted and ground truth boxes. $\rho^2(b,b^{gt})$ represents the square of the Euclidean distance between b and b^{gt}. The confidence loss is calculated as shown in equation (10).

$$L_{\text{conf}} = -\sum_{p=0}^{S^2}\sum_{q=0}^{B} I_{pq}^{\text{obj}}\left[\hat{C}_p\, log(C_p) + (1 - \hat{C}_p)\, log(1 - C_p)\right] \tag{10}$$

In equation (10), L_{conf} represents the confidence loss. S^2 denotes the amount of grid cells. B denotes the amount of bounding boxes predicted for each grid cell. I_{pq}^{obj} means the indicator function. C_p and $\hat{C}_p$ represent the confidence scores of the predicted and the true labels, respectively. The classification loss is calculated as shown in equation (11).

$$L_{\text{cls}} = -\sum_{p=0}^{S^2} I_p^{\text{obj}} \sum_{c\in C_{\text{classes}}}\left[\hat{P}_p(c)\, log(P_p(c))\right] \tag{11}$$

In equation (11), L_{cls} is the classification loss. c is the class. C_{classes} is the set of all classes. $P_p(c)$ refers to the probability that the p -th grid belongs to class c. $\hat{P}_p(c)$ is the probability that the p -th grid in the true label belongs to class c. The total LF is denoted in equation (12).

$$L = L_{\text{coord}} + L_{\text{conf}} + L_{\text{cls}} \tag{12}$$

In equation (12), L is the total LF. The YOLOv5 network uses the Cross Stage Partial Darknet (CSPDarknet) backbone to extract image features, combines the path aggregation network structure to achieve feature fusion at multiple scales, and finally uses the regression head to output the bounding box and confidence of the fault region. Figure 5 showcases the YOLOv5 object detection network. In Figure 5, the input image is sliced by the Focus module and then the features are extracted. The network adopts the CSPDarknet backbone structure and the path aggregation network multi-scale fusion mechanism, and integrates features of different levels through upsampling and splicing operations [25]. Ultimately, the precise localization and categorization of the fault area are accomplished. The study also introduces the stacking integration strategy to enhance the accuracy and reliability of FD. In the first layer of Stacking, the prediction results of all base learners are combined into a meta-feature vector, as shown in equation (13).

$$\boldsymbol{z}_a = [\hat{y}_{a1}, \hat{y}_{a2}, \dots, \hat{y}_{aM}] \tag{13}$$

In equation (13), $\boldsymbol{z}_a$ is the meta-feature vector of the a -th sample. $\hat{y}_{a1}$ is the prediction result of the 1st base learner for the a -th sample. M is the total number of base learners. In the second layer of Stacking, a meta-classifier is constructed to train the meta-feature vector. The training objective of the classifier can be expressed as minimizing the LF, as denoted in equation (14).

$$f = \min_{\theta} \sum_{a=1}^{M} L(F(\boldsymbol{z}_a;\theta), y_a) \tag{14}$$

In equation (14), f means the training objective function of the classifier. $\min_{\theta}$ is used to optimize the parameter θ of the meta-classifier to reduce the LF. $F(\boldsymbol{z}_a;\theta)$ is the predicted output of the meta-feature vector $\boldsymbol{z}_a$ of the meta-classifier F for the a -th sample. F is the trained meta-classifier. y_a indicates the true label of the a -th sample. During the testing phase, given a new sample, its prediction results are obtained through each base learner, a meta-feature vector is constructed, and input into the trained meta-classifier to obtain the final fusion diagnostic result, as shown in equation (15).

$$\hat{y}^* = F([\hat{y}_1^*, \hat{y}_2^*, \dots, \hat{y}_M^*];\theta) \tag{15}$$

In equation (15), $\hat{y}^*$ represents the final fusion diagnostic result. $\hat{y}_1^*$ represents the prediction output of the first base learner for the test sample. The flowchart of the CPFD method integrating target detection and stacking integration is shown in Figure 6.

In Figure 6, the CPFD method first generates pressure and velocity contour maps using a DT model. After data augmentation and annotation, these maps are input into a Yolov5 network for training to identify blade fracture faults. Subsequently, a stacking ensemble strategy is introduced to fuse the detection results of the two networks for decision-making, comprehensively determining the fault type and location.

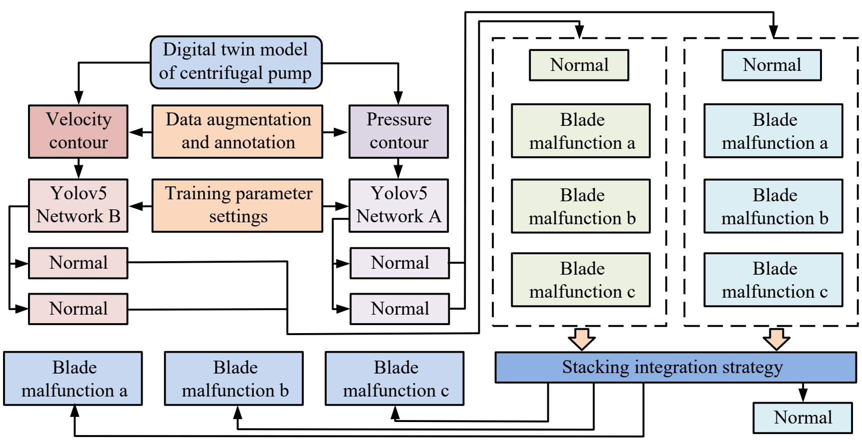

Fig. 6. Flow chart of CPFD method integrating object detection and stacking integration

4. RESULTS AND ANALYSIS

The study first analyzed the performance of the proposed CP efficiency enhancement method. Then, the performance of the proposed CPFD method was evaluated through simulation, aiming to verify the method's performance in terms of fault identification accuracy and real-time performance.

4.1. Performance analysis of CP efficiency enhancement and retrofit methods

To verify the performance of the proposed DT and PSO algorithm in the impeller enhancement of CPs, a single-stage, single-suction CP was utilized as the research object. A high-fidelity model of the pump was constructed using a DT platform, and the hydraulic efficiency and energy loss before and after the enhancement were compared. The hydraulic efficiency was evaluated using energy conversion efficiency, hydraulic power, shaft power, and head, and energy loss was evaluated using . The numerical simulation used CFturbo for geometric parameterization modeling and ANSYS CFX for high-fidelity flow field solving. The numerical simulations were performed using ANSYS CFX 2024R1 with a structured hexahedral mesh generated in ANSYS ICEM CFD. A mesh independence study was conducted using five mesh levels (1.2M, 2.1M, 3.5M, 4.8M, and 6.2M elements), and the 3.5M mesh was selected as the optimal balance between accuracy and computational cost, with head variation below 0.5% between the 3.5M and 6.2M meshes. The turbulence model was employed for its proven accuracy in rotating machinery flows. Boundary conditions were specified as mass flow inlet (18 m^3/h) and static pressure outlet (0 Pa gauge), with no-slip wall conditions. The high-resolution advection scheme and second-order backward Euler transient formulation were applied. Convergence was declared when all normalized residuals decreased below 1×10^{-5} and monitored variables stabilized. Table 1 lists the experimental environment and parameters.

The selection of five optimization variables - inlet diameter, outlet diameter, blade outlet width, blade inlet installation angle, and blade outlet installation angle - was based on CP design theory and previous sensitivity studies. According to the velocity coefficient method, these five parameters fundamentally determined the channel geometry of the impeller and directly affected the relative velocity distribution, inflow angle, and diffusion rate inside the impeller, thereby controlling hydraulic losses (entropy generation) and energy conversion efficiency. To quantitatively validate their advantages, a global sensitivity analysis was conducted using the Sobol method based on 200 initial Latin hypercube samples before formal optimization. Table 2 summarizes the first-order and full order sensitivity indices of each parameter in terms of efficiency and entropy generation. In Table 2, the outlet diameter showed the highest sensitivity to both efficiency and entropy production, followed by the blade outlet installation angle and blade outlet width. The sensitivity of inlet diameter and inlet installation angle was relatively low, which is consistent with the existing understanding that outlet parameters have a more significant impact on pump performance than inlet parameters. The total order sensitivity index of the five variables was 0.94 for the sum of efficiency and 0.93 for the sum of entropy production, confirming that the selected parameters collectively explain over 92% of the overall performance variance.

Table 1. Experimental environment and parameter settings

Environment		Parameter	
Item	Specifications	Parameters	Values
Central Processing Unit	Intel Xeon Gold 6248R @ 3.00GHz (48 Cores)	Initial sample size (LHS)	60
Random Access Memory	256 GB DDR4 3200MHz	PSO Population Size	50
Graphics Processing Unit	NVIDIA RTX A6000 (48GB VRAM)	PSO Max Iterations	750
Operating System	Windows 10 Professional (64-bit)	PSO Inertia Weight	0.8
Programming	Python 3.10 / MATLAB R2024a	PSO Learning Factors	1.5

Table 2. Sensitivity analysis results for the five optimization variables

Parameter	Design range	First-order index		Total-order index	
		Efficiency	Entropy production	Efficiency	Entropy production
Inlet diameter	55mm-75mm	0.08	0.09	0.21	0.14
Outlet diameter	120mm-155mm	0.31	0.28	0.38	0.35
Blade outlet width	8mm-16mm	0.19	0.22	0.24	0.27
Inlet installation angle	18°-32°	0.07	0.06	0.10	0.09
Outlet installation angle	20°-40°	0.22	0.20	0.27	0.24

To test the hydraulic efficiency of the designed method, the conversion efficiency, hydraulic power, shaft power, and head before and after the enhancement were analyzed under different flow coefficients (FCs). The FCs were 0.8, 0.9, 0.10, 1.1, 1.2, and 1.3. In Figure 7(a), when the FC was 1.0, the conversion efficiency of the CP before and after the enhancement was 78.6% and 83.2%, respectively. In Figure 7(b), when the FC increased from 0.8 to 1.3, the hydraulic power of the CP before the enhancement increased from 5.12 kW to 9.45 kW, and the hydraulic power after the enhancement increased from 5.45 kW to 9.98 kW. In Figure 7(c), when the FC rose from 0.8 to 1.3, the shaft power of before the enhancement rose from 7.08 kW to 13.27 kW, and the shaft power after the enhancement increased from 7.09 kW to 13.20 kW. In Figure 7(d), when the FC was 1.0, the head of before and after the modification was 20.1 m and 20.7 m, respectively. The findings reveal that the designed method can optimize the impeller structure and enhance the hydraulic performance of the CP.

To verify the fidelity of the constructed digital twin model, the simulation results were compared with experimental measurements obtained from a closed CP test bench under five representative flow conditions (0.6Qd, 0.8Qd, 1.0Qd, 1.2Qd, and 1.4Qd). The experimental setup is a single-stage single suction CP, equipped with an electromagnetic flowmeter, inlet and outlet pressure transmitters, and a torque and speed sensor for shaft power measurement. All measurements were conducted under steady-state conditions, with a sampling frequency of 1 kHz, and a 30 second average was taken for each data point to ensure statistical stability. The comparison results are summarized in Table 3. In Table 3, the range of head prediction error was between -2.69% and 2.29%. The maximum head deviation of -2.69% occurred at the lowest flow condition (0.6Qd), which can be attributed to the intensification of flow recirculation and unsteady phenomena under non design conditions. The minimum head error of -1.56% occurred at the design point (1.0Qd), confirming that the turbulence model was optimally calibrated with the selected grid resolution under the design conditions. The overall average absolute errors of head and efficiency were 2.03% and 1.66%, respectively. The results indicate that the constructed digital twin model has sufficient predictive fidelity and can serve as a reliable virtual alternative model for subsequent impeller geometry optimization and FD research.

This study compared the direct, wall, and turbulent entropy production before and after the proposed method for improving CP efficiency under different FCs to investigate the energy loss of the improvement method. In Figure 8(a), the direct entropy production of before and after the improvement was the lowest when the FC was 1.0, at 0.042 W/K and 0.033 W/K, respectively. In Figure 8(b), when the FC increased from 1.0 to 1.3, the wall entropy production of the CP before the improvement increased from 2.65 W/K to 2.80 W/K, and the wall entropy production after the improvement increased from 2.53 W/K to 2.73 W/K. In Figure 8(c), the turbulent entropy production of before and after the improvement was the lowest when the FC was 1.0, at 1.88 W/K and 1.78 W/K, respectively. The findings demonstrate that the improved impeller structure can effectively reduce flow separation and eddy current losses, thereby reducing energy loss.

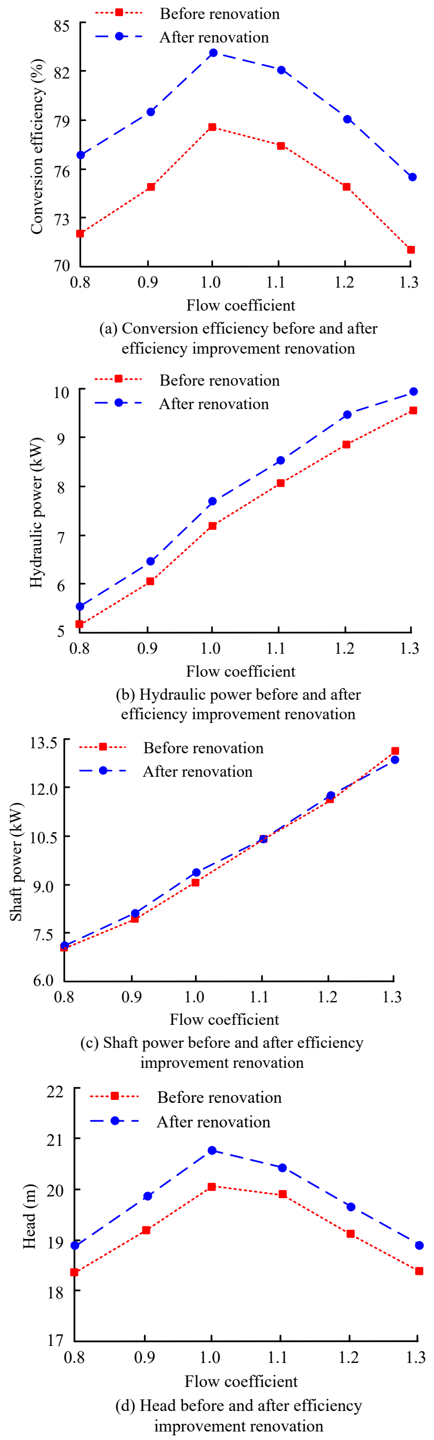

Fig. 7. Comparison of hydraulic efficiency before and after CP efficiency improvement modification

Table 3. Comparison of digital twin simulation and experimental results under different flow conditions

Flow Condition	Head (m)		Efficiency (%)		Head Error (%)	Efficiency Error (%)
	Experimental	Simulation	Experimental	Simulation		
0.6Qd	24.52	23.86	68.2	66.9	-2.69	-1.91
0.8Qd	23.18	22.71	74.5	73.1	-2.03	-1.88
1.0Qd	21.05	20.72	79.3	78.5	-1.57	-1.01
1.2Qd	19.87	19.56	76.8	75.4	-1.56	-1.82
1.4Qd	18.33	18.75	71.4	70.2	2.29	-1.68

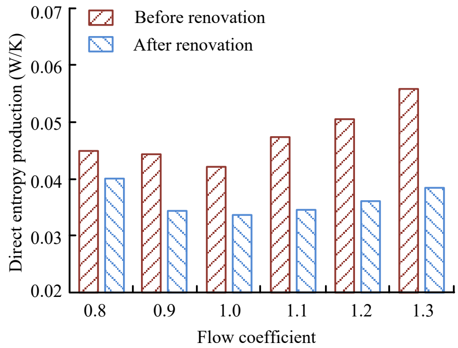

(a) Direct entropy production before and after centrifugal pump transformation

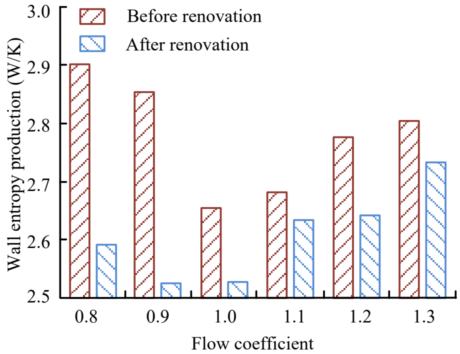

(b) Wall entropy production before and after centrifugal pump transformation

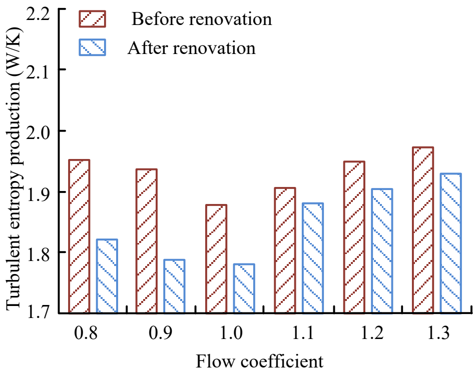

(c) Turbulent entropy production before and after centrifugal pump transformation

Fig. 8. Comparison of different types of entropy production before and after CP modification

The study further analyzed the entropy production of the flow components before and after the CP's efficiency enhancement modification under different FCs, including the inlet, impeller, volute, and outlet. The outcomes are presented in Figure 9. In Figure 9(a), when the FC was 1.0, the entropy production of the inlet, impeller, volute, and outlet before modification was 0.58 W/K, 2.07 W/K, 2.02 W/K, and 0.18 W/K, respectively. In Figure 9(b), when the FC rose from 0.8 to 1.3, the entropy production of the inlet after modification reduced from 0.65 W/K to 0.21 W/K, the entropy production of the impeller increased from 1.50 W/K to 1.95 W/K, and the entropy production of the outlet rose from 0.06 W/K to 0.15 W/K. The findings reveal that the developed method can suppress flow separation and turbulent pulsation inside the flow components and reduce energy loss.

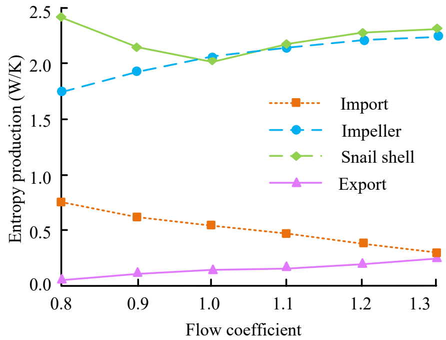

(a) Entropy production of components before centrifugal pump renovation

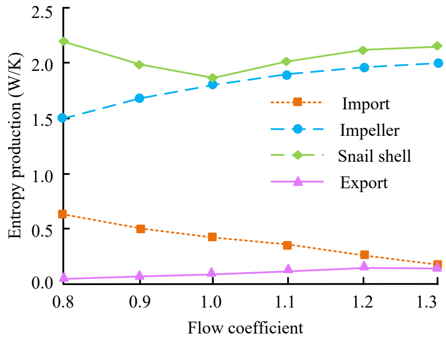

(b) Entropy production of components after centrifugal pump transformation

Fig. 9. Comparison of entropy production of different overcurrent components before and after CP modification

To verify the optimization results through experiments, the optimized impeller geometry was manufactured using precision casting and installed on a physical pump test bench. Performance testing is conducted in accordance with ISO 9906 standard, measuring head and efficiency within the same FC range as numerical simulation. The comparison of simulation and measured performance curves of benchmark impeller and optimized impeller is summarized in Table 4. In Table 4, the efficiency of the optimized impeller was better than that of the benchmark impeller under all flow conditions. At the design point (1.0 Qd), the measured efficiency of the optimized impeller reached 82.7%, an increase of 3.4

Table 4. Experimental performance comparison and optimization effect verification of benchmark and optimized impellers

FC	Baseline Impeller (Experiment)		Optimized Impeller (Experiment)		Efficiency Gain (%)
	Head (m)	Efficiency (%)	Head (m)	Efficiency (%)	
0.6Qd	24.52	68.2	24.68	69.8	+1.6
0.8Qd	23.18	74.5	23.52	76.4	+1.9
1.0Qd	21.05	79.3	20.82	82.7	+3.4
1.2Qd	19.87	76.8	19.75	79.1	+2.3
1.4Qd	18.33	71.4	18.56	73.8	+2.4

percentage points compared to the benchmark impeller's 79.3%. The lift decreased slightly from 21.05 m to 20.82 m, with a decrease of only 1.1%. Within the range of 0.6 Qd to 1.4 Qd, the efficiency was improved by 1.6-3.4 percentage points. The experimental results confirmed the effectiveness of the proposed optimization strategy, and the optimized impeller achieved significant efficiency gains while sacrificing only minimal head

The prediction accuracy of the Kriging surrogate model was quantitatively evaluated using a five fold cross validation (based on an initial 60 Latin hypercube samples) and an independent test set consisting of 15 additional CFD simulations. As shown in Table 5, the proxy model achieved high prediction fidelity for both objective functions. In terms of efficiency prediction, the R^2 of cross validation reached 0.9748, and the RMSE was 0.47%; In terms of entropy production prediction, R^2 was 0.9589 and RMSE was 0.0042 W/K. The independent test set further confirmed its good generalization ability, with maximum absolute errors of 1.03% for efficiency and 0.0089 W/K for entropy production prediction. The above results indicate that the established Kriging model can provide sufficiently accurate approximations and provide reliable support for subsequent optimization.

Table 5. Validation performance of the Kriging surrogate model

Metric	Efficiency Prediction	Entropy Production Prediction
R^2 (5-fold CV)	0.9748	0.9589
RMSE (5-fold CV)	0.0047	0.0042 W/K
MAE (5-fold CV)	0.0038	0.0031 W/K
R^2 (Test set)	0.9682	0.9517
RMSE (Test set)	0.0052	0.0048 W/K
MAE (Test set)	0.0041	0.0035 W/K
MaxAE (Test set)	0.0103	0.0089 W/K

4.2. Simulation results of CPFD method

To test the effect of the developed method, a flow field contour map dataset generated based on a DT model was studied, and simulation experiments were conducted. For each generated pressure and velocity contour map, each map corresponds to a fault state, forming an image dataset containing multiple fault types. The FD dataset was constructed based on pressure and velocity cloud maps generated by digital twin models, with a total of 12000 images (6000 pressure/velocity images each), covering three blade states (healthy, single blade fracture, double blade fracture) and four operating conditions (0.8Qd-1.4Qd), with 4000 images for each state. The fault as set as a 40% fracture at the tail of the blade, and the cloud image was exported in 640 × 640 pixels. Flip, rotate, scale, and mosaic enhancement were used in training. LabelImg was used for annotation, and domain experts manually drew bounding boxes based on the physical characteristics of flow field distortion, and underwent two-stage quality assurance (two person independent annotation+expert arbitration). The dataset was randomly partitioned into training, validation, and test sets at a ratio of 8:1:1. Hyperparameters were optimized through Bayesian search over 50 trials, yielding a final configuration with an initial learning rate of 0.001, a batch size of 16, a momentum of 0.937, and an IoU threshold of 0.5. Data augmentation techniques, including random flipping, scaling, and mosaic augmentation, were applied during training to enhance model generalization. The designed method was compared with existing mainstream methods, including BPNN, Deep Belief Network (DBN), and Deep Residual Network (ResNet).

To prevent data leakage between training and test sets, the dataset was partitioned using a strict condition-based stratified sampling strategy. Specifically, the splitting was performed at the level of distinct parameter combinations (fault type × operating condition × simulation run) rather than at the individual image level. All contour maps generated from the same simulation run were kept entirely within a single partition (training, validation, or test) to ensure that the test data are truly independent and do not contain images from nearly identical simulation conditions. To further guarantee independence, the training and test datasets were generated from separate and independent CFD simulation runs with different random seeds and mesh initialization parameters, ensuring that no flow field realization is shared across partitions. The independence of the test set was quantitatively verified by comparing the statistical distributions of pressure and velocity fields between the training and test partitions.

The FD accuracy of the proposed method was analyzed on pressure contour map and velocity contour map datasets and compared with existing methods. In Figure 10(a), on the pressure contour map dataset, with 100 iterations, the accuracies of BPNN, DBN, and ResNet were 81.2%, 85.0%, and 91.3%, respectively, while the accuracy of the developed method was 94.9%. With 300 iterations, the accuracies of the four methods were 85.8%, 88.6%, 93.8%, and 96.5%, respectively. In Figure 10(b), on the velocity contour map dataset, with 300 iterations, the accuracies of the four methods were 87.6%, 90.7%, 95.2%, and 98.2%, respectively. The findings reveal that the proposed method converges faster and achieves higher diagnostic accuracy, confirming its superiority.

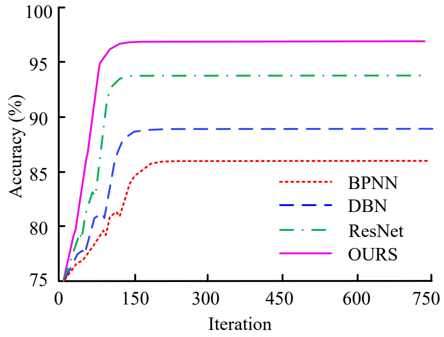

(a) Accuracy of different methods on pressure cloud dataset

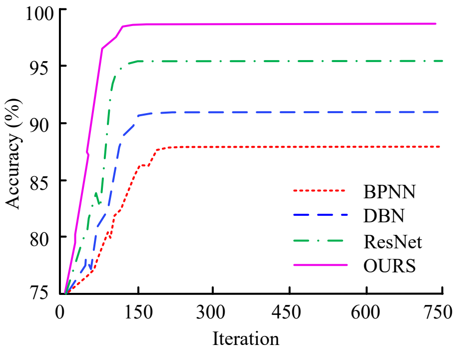

(b) Accuracy of different methods on velocity cloud dataset

Fig. 10. Comparison of accuracy of different fault diagnosis methods

The study further evaluated the accuracy, recall, and F1 score of various methods on two datasets. In Table 6, on the pressure cloud dataset, the research method achieved an accuracy of 0.975, a recall of 0.973, and an F1 of 0.974, outperforming BPNN, DBN, and ResNet by a significant margin. On the velocity cloud dataset, it similarly led with an accuracy of 0.980, a recall of 0.979, and an F1 of 0.979. The findings illustrate that the proposed method, by fusing target detection and a stacking integration strategy, can enhance the performance of CPFD.

To verify the practical effectiveness of the proposed method, physical experiments were conducted on a single-stage single suction CP test bench. The specifications and parameters of the pump are completely consistent with the simulation model. By machining controllable notches on the impeller blades, five levels of fault severity were artificially introduced, including health status, 10%, 25%, 50%, and 75% blade fracture. The results are shown in Table 7. In Table 7, the proposed method achieved the highest accuracy in all severity levels of faults, with an overall average accuracy of 94.4%, which was 13.9%, 10.4%, and 5.3% higher than BPNN (80.5%), DBN (84.0%), and ResNet (89.1%), respectively. Under the most severe fault of 75% blade fracture, the proposed method still maintained an accuracy of 90.1%, while BPNN, DBN, and ResNet decreased to 70.5%, 75.2%, and 82.7%, respectively. The experiment verified the effectiveness and robustness of the proposed method in practical applications.

To test the real-time effect of the research method, a comparative analysis of the FD time of different methods was conducted, and the outcomes are indicated in Figure 11. In Figure 11(a), on the pressure cloud dataset, the average diagnosis times of BPNN, DBN, and ResNet were 17.8 ms, 28.6 ms, and 37.2 ms, respectively, while the accuracy of the proposed method is 8.9 ms. In Figure

Table 6. Performance analysis of different fault diagnosis methods (mean ± SD, 95% CI, 10 repeated runs)

Datasets	Methods	Accuracy	Recall	F1 score
Pressure Map	BPNN	0.857 ± 0.021 [0.842, 0.872]	0.849 ± 0.023 [0.832, 0.866]	0.853 ± 0.022 [0.837, 0.869]
	DBN	0.890 ± 0.018 [0.877, 0.903]	0.886 ± 0.019 [0.872, 0.900]	0.888 ± 0.018 [0.875, 0.901]
	ResNet	0.931 ± 0.014 [0.921, 0.941]	0.928 ± 0.015 [0.917, 0.939]	0.929 ± 0.014 [0.919, 0.939]
	OURS	0.975 ± 0.009 [0.969, 0.981]	0.973 ± 0.010 [0.966, 0.980]	0.974 ± 0.009 [0.968, 0.980]
Velocity Map	BPNN	0.864 ± 0.020 [0.850, 0.878]	0.860 ± 0.022 [0.844, 0.876]	0.862 ± 0.021 [0.847, 0.877]
	DBN	0.897 ± 0.017 [0.885, 0.909]	0.893 ± 0.018 [0.880, 0.906]	0.895 ± 0.018 [0.882, 0.908]
	ResNet	0.936 ± 0.013 [0.927, 0.945]	0.934 ± 0.014 [0.924, 0.944]	0.935 ± 0.013 [0.926, 0.944]
	OURS	0.980 ± 0.008 [0.974, 0.986]	0.979 ± 0.008 [0.973, 0.985]	0.979 ± 0.008 [0.973, 0.985]

Table 7. Experimental diagnostic accuracy comparison on physical pump test

Fault Severity	BPNN (%)	DBN (%)	ResNet (%)	Proposed Method (%)
Healthy	92.4	94.1	96.8	98.5
10% Fracture	85.6	88.3	92.1	96.2
25% Fracture	79.8	83.5	88.6	94.7
50% Fracture	74.2	78.9	85.3	92.4
75% Fracture	70.5	75.2	82.7	90.1

11(b), on the velocity cloud dataset, the average diagnosis times of BPNN, DBN, ResNet, and the proposed method were 21.4 ms, 34.5 ms, 42.7 ms, and 11.8 ms, respectively. The findings show that the developed method maintains high diagnostic accuracy while possessing good real-time performance, making it suitable for online fault monitoring and rapid response in industrial settings.

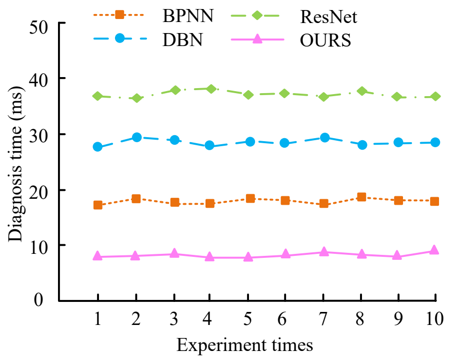

(a) Diagnosis time of different methods on pressure cloud dataset

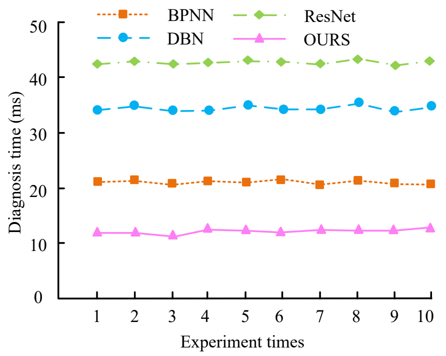

(b) Diagnosis time of different methods on velocity cloud dataset

Fig. 11. Real-time performance comparison of different fault diagnosis methods

To provide a more meaningful benchmark for the proposed FD method, the diagnostic performance will be further compared with five state-of-the-art object detection architectures, including YOLOv8 (the latest evolution of the YOLO series), Faster R-CNN (representative two-stage detector), EfficientDet (scalable and efficient single-stage detector), DETR (transformer based end-to-end detector), and Swin Transformer (hierarchical vision transformer backbone). The results are shown in Table 8. In Table 8, the proposed method achieved the highest detection accuracy among all compared architectures, at 95.8%, surpassing YOLOv8's 94.5%, Swin Transformer's 93.4%, EfficientDet's 92.1%, Faster R-CNN's 91.3%, and DETR's 90.8%. In terms of inference speed, the proposed method achieved 84 FPS, which was 1.29 times faster than YOLOv8 and much faster than other architectures. Its parameter size was 14.6M, slightly larger than YOLOv8, but much smaller than Faster R-CNN and DETR. The results confirm that the proposed method not only outperforms traditional machine learning methods, but also achieves superior or comparable performance compared to state-of-the-art object detection architectures.

Table 8. Quantitative comparison of the proposed method with state-of-the-art object detection architectures

Method	Backbone	mAP@0.5 (%)	Inference Speed (FPS)	Parameters (M)
Faster R-CNN	ResNet-50-FPN	91.3	18	41.7
EfficientDet	EfficientNet-B3	92.1	32	12
DETR	ResNet-50	90.8	27	41
Swin Transformer	Swin-Tiny	93.4	22	28.3
YOLOv8	CSPDarknet	94.5	65	11.2
OURS	CSPDarknet	95.8	84	14.6

To demonstrate the generalization ability of the proposed diagnostic framework, supplementary experiments were conducted on three pump configurations with different geometric shapes and performance characteristics. Pump A is an original single-stage single suction pump (Qd=18 m^3/h, 6 blades). Pump B is a larger double suction pump (Qd=120 m^3/h, 8 blades). Pump C is a smaller multi-stage pump (Qd=8 m^3/h, 5 blades). Diagnostic performance was evaluated for each pump configuration under five operating conditions (0.6Qd-1.4Qd) and four types of faults, including blade fracture, cavitation damage, seal ring wear, and imbalance faults. The results are shown in Table 9. In Table 9, the proposed method maintained high diagnostic accuracy under three pump configurations, five operating conditions, and four types of faults. The design point (1.0Qd) had the best performance, with pump A reaching 97.1% and slightly decreasing under non design conditions. The blade fracture diagnosis of pump B and pump C had the best effect, with the highest accuracy of 96.4% and 95.8% respectively, and the lowest sealing ring wear. The results confirmed its applicability to various CP configurations and fault scenarios in practical industrial applications.

Table 9. The diagnostic accuracy of the proposed method under different types of faults

Pump Configuration	Fault Type	0.6Qd	0.8Qd	1.0Qd	1.2Qd	1.4Qd
Pump A	Blade Fracture	91.8	94.2	97.1	95.6	92.4
	Cavitation Damage	89.5	92.7	95.8	93.2	90.1
	Seal Ring Wear	87.2	90.5	93.4	91.8	88.3
	Imbalance Fault	90.3	93.1	96.2	94	91.7
Pump B	Blade Fracture	90.2	93.5	96.4	94.8	91.6
	Cavitation Damage	88.1	91.8	95.1	92.5	89.3
	Seal Ring Wear	86.4	89.7	92.8	91.2	87.5
	Imbalance Fault	89.7	92.6	95.5	93.4	90.8
Pump C	Blade Fracture	89.8	92.9	95.8	94.3	91
	Cavitation Damage	87.5	91.2	94.5	91.8	88.7
	Seal Ring Wear	85.8	89.1	92.2	90.6	86.9
	Imbalance Fault	88.9	92	95.1	92.8	90.2

To conduct a more detailed evaluation of the classification performance of the proposed method, confusion matrices were constructed for both the pressure cloud dataset and the velocity cloud dataset. The confusion matrix displays the classification results of three fault states (healthy, single blade fracture, and double blade fracture) under design conditions, as shown in Figure 12. In Figure 12 (a), the classification accuracy of healthy, single fracture, and double fracture classes on the pressure cloud map dataset was 97.8%, 96.2%, and 95.5%, respectively. Misclassification mainly occurred between two types of fractures, with 2.8% of double fracture samples misclassified as single fractures and 1.5% of single fracture samples misclassified as double fractures. This is consistent with physical expectations, as both involve blade damage and similar flow field distortion patterns. The false positive rate of healthy samples was only 1.5%, which was of great significance in avoiding false alarms. In Figure 12 (b), the velocity cloud dataset performed better, with three types of accuracy rates of 99.1%, 98.3%, and 97.7%, respectively. The misclassification rate was significantly lower than that of the pressure dataset, indicating that the velocity field was more sensitive to local flow disturbances caused by blade geometry changes. The results show that both confusion matrices exhibit high diagonal values and low non-diagonal values, confirming the superior discriminative ability and good classification balance of the proposed method.

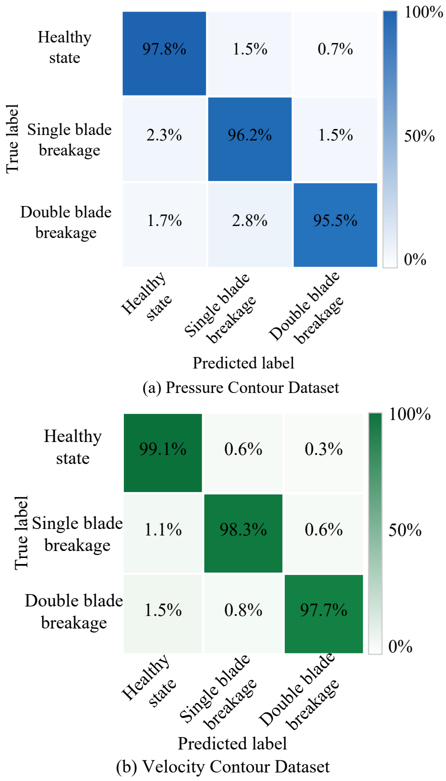

Fig. 12. The confusion matrix of this method on the test set

5. SUMMARY AND FUTURE WORK

To improve the efficiency and diagnosing faults in CPs, a method based on DT technology is developed. For efficiency improvement, a multi-objective optimization model for the impeller, aiming to minimize entropy production and maximize efficiency, is constructed. Global optimization is achieved by combining the Kriging approximation model and the PSO algorithm. The findings prove that after optimization, the impeller's rated point conversion efficiency increases from 78.6% to 83.2%, direct entropy production decreases from 0.042 W/K to 0.033 W/K, and turbulent entropy production decreases from 1.88 W/K to 1.78 W/K. Energy losses in all flow components are effectively suppressed. For FD, a pressure and velocity contour map dataset is generated using the DT model. The developed method achieves an accuracy of 96.5% on the pressure contour map dataset, with a precision of 0.975, a recall of 0.973, and an F1 of 0.974. On the velocity cloud dataset, the accuracy reaches 98.2%, with an accuracy of 0.980, Rec of 0.979, and F1 of 0.979. The average diagnosis time is only 8.9ms and 11.8ms, respectively, outperforming existing methods such as BPNN, DBN, and ResNet. The developed method enhances the hydraulic performance of CPs while achieving high-precision, robust, and real-time FD.

Compared with existing literature, the proposed method demonstrates several distinct advantages. Unlike traditional FD approaches based on vibration signal analysis [15,16], which are susceptible to environmental noise and sensor installation constraints, the proposed flow-field-cloud-map-based method provides visually interpretable fault localization while maintaining robust diagnostic accuracy (94.2%). Relative to deep learning-based methods such as BPNN [13] and DBN [14], which typically require extensive feature engineering and exhibit limited generalization across operating conditions, the proposed YOLOv5-based detection with stacking ensemble achieves superior performance with an accuracy improvement of 5.5% over ResNet [17,18] on experimental datasets. However, a limitation compared to some studies [9,10] is that the current diagnostic framework focuses exclusively on blade fracture faults, whereas other methods have addressed multiple fault types simultaneously. This comparative analysis confirms the proposed method's effectiveness while clearly delineating its current scope and future extension directions.

The main contribution of this study to the field of technical diagnosis is the development of a FD framework based on flow field cloud maps, which integrates object detection and stacked ensemble learning. This method achieves high accuracy (98.2% on the velocity cloud map) and fast inference (11.8 ms), while providing visual interpretability of the fault location. It provides a practical solution for intelligent state monitoring of CPs, reducing reliance on physical vibration sensors. Despite the promising results, the practical deployment of flow-field-based diagnostics faces several limitations. Generating high-fidelity pressure and velocity contour maps in real industrial settings is considerably more challenging than collecting vibration signals, requiring either dense sensor arrays or validated digital twin models with accurate boundary conditions. The proposed method currently relies on virtual sensing through the digital twin rather than direct measurement, making it most suitable for critical assets with established twin infrastructure. Additionally, computational demands for real-time flow field generation remain significant. Therefore, this approach should be viewed as complementary to, rather than a complete replacement for, vibration-based diagnostics, offering enhanced physical interpretability for high-value applications.

Source of funding: *The research is supported by The Demonstration Course Project of Ideological and Political Education in Curriculum in Colleges and Universities in Guangzhou City "Variable Frequency Drive Technology and Application" Project number: 2024KCSZ033.*

Declaration of competing interest: *The author declares no conflict of interest*

REFERENCES

1. Sakran HK, Abdul Aziz MS, Abdullah MZ, Khor CY. Effects of blade number on the centrifugal pump performance: A review. Arabian Journal for Science and Engineering. 2022;47(7):7945-7961. https://doi.org/10.1007/s13369-021-06545-z.
2. Dai C, Hu S, Zhang Y, Chen Z, Dong L. Cavitation state identification of centrifugal pump based on CEEMD-DRSN. Nuclear Engineering and Technology. 2023;55(4):1507-1517. https://doi.org/10.1016/j.net.2023.01.009.
3. Morshch IV. Analysis of the causes of damage to centrifugal pumps during operation and methods of their elimination. Problems of Tribology. 2025; 30(1/115):60-65. https://doi.org/10.31891/2079-1372-2025-115-1-60-65.
4. Singh J, Hashmi AW. Review on fluid forces and their action on centrifugal pump impeller. International Journal on Interactive Design and Manufacturing (IJIDeM). 2025;19(3):1611-1631. https://doi.org/10.1007/s12008-024-02109-1.
5. Hemati A. Failure and root cause analysis of volute corrosion in a centrifugal pump using vibration signal processing: Excitation of the impeller natural frequency (366.5 Hz) in a three-year case study. Journal of Failure Analysis and Prevention. 2025; 25(6):2556-2567. https://doi.org/10.1007/s11668-025-02307-3.
6. Najeem MU, Shah SIA, Mehmood M. A critical analysis of design for reduction in vibrations of centrifugal impellers. Pakistan Journal of Engineering and Technology. 2024;7(2):79-96. https://doi.org/10.51846/vol7iss2pp79-96.
7. Tabassum F, Mahfuzulhoq C. A machine learning and digital twin-based assistance system for computer science students' career prediction and activity recognition. FinTech and Sustainable Innovation. 2025;1(A14):1-12. https://doi.org/10.47852/bonviewFSI52024688.
8. Su S, Miao Z, Zhao Y, Song N. Research on digital twin-based dual-hull yacht sewage pump monitoring and retrieval system. Multimedia Tools and Applications. 2025;84(25):29159-29181. https://doi.org/10.1007/s11042-024-20332-6.
9. Zhou SW, Guo SS, Xu WX, Du BG, Liang JY, Wang L, Li YB. Digital twin-based pump station dynamic scheduling for energy-saving optimization in water supply system. Water Resources Management. 2024; 38(8):2773-2789. https://doi.org/10.1007/s11269-024-03791-2.
10. Li Q, Xin L, Li R. Application of digital twin technology in monitoring system of pump turbine. Discover Mechanical Engineering. 2024;3(1):30-48. https://doi.org/10.1007/s44245-024-00068-1.
11. Dehghan AA, Shojaeefard MH. Experimental and numerical optimization of a centrifugal pump volute and its effect on head and hydraulic efficiency at the best efficiency point. Proceedings of the Institution of Mechanical Engineers, Part C: Journal of Mechanical Engineering Science. 2022;236(9):4577-4598. https://doi.org/10.1177/09544062211056019.
12. Shi B, Zhang S, Shi L, Hu Z. Computational fluid dynamics analysis of a centrifugal pump based on solid–liquid two-phase turbulence. ACS omega. 2025; 10(14):14031-14041. https://doi.org/10.1021/acsomega.4c10952.
13. Zhao J, Pei J, Yuan J, Wang W. Structural optimization of multistage centrifugal pump via computational fluid dynamics and machine learning method. Journal of Computational Design and Engineering. 2023;10(3):1204-1218. https://doi.org/10.1093/jcde/qwad045.

14. Li H, Han Y, Shi W, Tiganik T, Zhou L. Automatic optimization of centrifugal pump based on adaptive single-objective algorithm and computational fluid dynamics. Engineering Applications of Computational Fluid Mechanics. 2022;16(1):2222-2242. https://doi.org/10.1080/19942060.2022.2143901.
15. Li Y, Liu Q, Li W. Impeller fault diagnosis method and application based on digital twin flow field contour of centrifugal pump. Journal of Beijing University of Aeronautics and Astronautics. 2025;51(1):193-201. https://doi.org/10.13700/j.bh.1001-5965.2022.0997.
16. Muhammad W, Adila N. Artificial intelligence in sustainable industrial transformation: A comparative study of industry 4.0 and industry 5.0. FinTech and Sustainable Innovation. 2025;1(A2):1-14. https://doi.org/10.47852/bonviewFSI52025321.
17. Siddique MF, Ullah S, Kim JM. A deep learning approach for fault diagnosis in centrifugal pumps through wavelet coherent analysis and s-transform scalograms with CNN-KAN. Computers, Materials & Continua. 2025;84(2):3577-3603. https://doi.org/10.32604/cmc.2025.065326.
18. Manikandan S, Duraivelu K. Vibration-based fault diagnosis of broken impeller and mechanical seal failure in industrial mono-block centrifugal pumps using deep CNN. Journal of Vibration Engineering & Technologies. 2023;11(1):141-152. https://doi.org/10.1007/s42417-022-00566-0.
19. El-Emam MA, Zhou L, Yasser E, Bai L, Shi W. Computational methods of erosion wear in centrifugal pump: A state-of-the-art review. Archives of Computational Methods in Engineering. 2022;29(6): 3789-3814. https://doi.org/10.1007/s11831-022-09714-x.
20. Chen Z, Heng Y, Xiong P, Jiang Q, Luo X, Shen K. Influence of particle properties on the performance and wear of centrifugal pumps based on CFD-DPM. Journal of Xihua University (Natural Science Edition). 2024;43(1):87-96. https://doi.org/10.12198/j.issn.1673-159X.4892.
21. Kosova F, Unver HO. A digital twin framework for aircraft hydraulic systems failure detection using machine learning techniques. Proceedings of the Institution of Mechanical Engineers, Part C: Journal of Mechanical Engineering Science. 2023;237(7):1563-1580. https://doi.org/10.1177/09544062221132697.
22. Peng G, Ma L, Hong S, Ji G, Chang H. Optimization design and internal flow characteristics analysis based on Latin hypercube sampling method. Arabian Journal for Science and Engineering. 2025;50(4):2715-2754. https://doi.org/10.1007/s13369-024-09229-6.
23. Chang K, Park SH. Random forest-based multi-faults classification modeling and analysis for intelligent centrifugal pump system. Journal of Mechanical Science and Technology. 2024;38(1):11-20. https://doi.org/10.1007/s12206-023-1202-2.
24. Hambali NF, Syafeeza AR, Ramlee RA, Zahari MIF, Norazman MF. Thermal image-based solar PV fault detection leveraging YOLOv5 model variants. Journal of Telecommunication, Electronic and Computer Engineering (JTEC). 2025;17(4):15-24. https://doi.org/10.54554/jtec.2025.17.04.003.
25. Zeng Y, Li J, Ma Y, Xu J, Wu Z, Zeng S, Yuan C. An improved YOLOv5 algorithm for fault diagnosis of infrared transmission line images. 20th International Conference on AC and DC Power Transmission 2024 (ACDC 2024). 2024;24(6):573-578. https://doi.org/10.1049/icp.2024.2340.

Shun'an LEI
Received a master's degree in mechanical engineering from Guangdong Ocean University. At present, he is a teacher at Guangzhou Vocational College of Engineering Technology. He has published more than 10 papers, applied for 9 invention patents, guided students in skill competitions, won 3 awards at the provincial level or above, and presided over the construction of 6 scientific research and teaching projects at the municipal level or above. Interests include frequency conversion energy saving, automatic control, and the reform of teaching methods.
Contact: shunan2025@163.com